



Constraining the Nature of the 18 min Periodic Radio Transient GLEAM-X J162759.5-523504.3 via Multiwavelength Observations and Magneto-thermal Simulations

N. Rea^{1,2} , F. Coti Zelati^{1,2} , C. Dehman^{1,2} , N. Hurley-Walker³ , D. De Martino⁴ , A. Bahramian³ ,
D. A. H. Buckley^{5,6} , J. Brink^{5,6} , A. Kawka³ , J. A. Pons⁷ , D. Viganò^{1,2} , V. Graber^{1,2} , M. Ronchi^{1,2} ,
C. Pardo Araujo^{1,2} , A. Borghese^{1,2} , E. Parent^{1,2} , and T. J. Galvin^{3,8}

¹ Institute of Space Sciences (ICE), CSIC, Campus UAB, Carrer de Can Magrans s/n, E-08193, Barcelona, Spain; rea@ice.csic.es

² Institut d'Estudis Espacials de Catalunya (IEEC), Carrer Gran Capità 2–4, E-08034 Barcelona, Spain

³ International Centre for Radio Astronomy Research, Curtin University, Kent St, Bentley, WA 6102, Australia

⁴ INAF—Osservatorio Astronomico di Capodimonte, Salita Moiarriello 16, I-80131 Napoli, Italy

⁵ South African Astronomical Observatory, PO Box 9, Observatory Road, Observatory 7935, Cape Town, South Africa

⁶ Department of Astronomy, University of Cape Town, Private Bag X3, Rondebosch 7701, South Africa

⁷ Departament de Física Aplicada, Universitat d'Alacant, E-03690 Alicante, Spain

⁸ CSIRO, Space and Astronomy, P.O. Box 1130, Bentley, WA 6102, Australia

Received 2022 June 28; revised 2022 October 4; accepted 2022 October 4; published 2022 November 22

Abstract

We observed the periodic radio transient GLEAM-X J162759.5-523504.3 (GLEAM-X J1627) using the Chandra X-ray Observatory for about 30 ks on 2022 January 22–23, simultaneously with radio observations from the Murchison Widefield Array, MeerKAT, and the Australia Telescope Compact Array. Its radio emission and 18 min periodicity led the source to be tentatively interpreted as an extreme magnetar or a peculiar highly magnetic white dwarf. The source was not detected in the 0.3–8 keV energy range with a 3σ upper limit on the count rate of 3×10^{-4} counts s^{-1} . No radio emission was detected during our X-ray observations either. Furthermore, we studied the field around GLEAM-X J1627 using archival European Southern Observatory and DECam Plane Survey data, as well as recent Southern African Large Telescope observations. Many sources are present close to the position of GLEAM-X J1627, but only two within the $2''$ radio position uncertainty. Depending on the assumed spectral distribution, the upper limits converted to an X-ray luminosity of $L_X < 6.5 \times 10^{29}$ erg s^{-1} for a blackbody with temperature $kT = 0.3$ keV, or $L_X < 9 \times 10^{29}$ erg s^{-1} for a power law with photon index $\Gamma = 2$ (assuming a 1.3 kpc distance). Furthermore, we performed magneto-thermal simulations for neutron stars considering crust- and core-dominated field configurations. Based on our multiband limits, we conclude that (i) in the magnetar scenario, the X-ray upper limits suggest that GLEAM-X J1627 should be older than ~ 1 Myr, unless it has a core-dominated magnetic field or has experienced fast cooling; (ii) in the white dwarf scenario, we can rule out most binary systems, a hot sub-dwarf, and a hot magnetic isolated white dwarf ($T \gtrsim 10,000$ K), while a cold isolated white dwarf is still compatible with our limits.

Unified Astronomy Thesaurus concepts: [Galactic radio sources \(571\)](#)

1. Introduction

The spin-period (P) evolution of a pulsar is driven by the combination of several factors: the presence of accretion during its lifetime either from supernova fall-back or a companion star, the dissipation of the magnetic field over time due to currents inside and outside the neutron star crust, the consumption of rotational energy via dipolar spin-down emission, occasional glitch events, etc (Lyne et al. 1985; Manchester & Taylor 1977). The population of rotational-powered radio pulsars has been observed to have spin periods in the range $P \sim 0.0014$ –12 s (Manchester et al. 2005). The majority of the observed population clusters around $P \sim 1$ s, with the extremes being populated on the fast side by rapidly spinning, recycled millisecond pulsars and on the slow side by magnetars. The spin distribution of classical magnetars (Kaspi & Beloborodov 2017; Esposito et al. 2021) ranges between ~ 1.4 s for Swift J1818.0–1607, a young radio magnetar recently discovered during an outburst (Esposito et al. 2020), and ~ 12 s for the bright, hard X-ray emitting magnetar

1E 1841–045 (Vasisht & Gotthelf 1997). However, the discovery of magnetar-like activity from the high-magnetic-field, rotation-powered pulsars PSR J1119–6127 ($P \sim 0.11$ s; Göğüş et al. 2016) and PSR J1846–0258 ($P \sim 0.3$ s; Gavril et al. 2008), as well as from 1E 161348-5055 at the center of the supernova remnant RCW103 ($P \sim 6.67$ hr; D’Ai et al. 2016; Rea et al. 2016), has enlarged the historical magnetar spin-period range. Furthermore, a few rotational-powered radio pulsars have been recently discovered with periods larger than the classical magnetar range: PSR J1903 + 0433 ($P \sim 14.1$ s; Han et al. 2021), PSR J0250 + 5854 ($P \sim 23.5$ s; Tan et al. 2018), and PSR J0901–4046 ($P \sim 76$ s; Caleb et al. 2022) (see also Figure 1).

On the other hand, the spin periods of magnetic white dwarfs range between ~ 0.019 and 10^4 hr (Brinkworth et al. 2013; Ferrario et al. 2020; Kilic et al. 2021). Magnetic white dwarfs have been observed both isolated (about 600 detected thus far) and in interacting binaries (about 200 detected), with magnetic fields reaching $\sim 10^9$ G. Periodic radio and optical emission has only been detected from the binary star AR Sco at the beat frequency between its spin and orbital periods (Marsh et al. 2016). The incoherent nature of the pulsed radio emission from AR Sco has pointed toward models involving particle acceleration due to the interaction between the two



Original content from this work may be used under the terms of the [Creative Commons Attribution 4.0 licence](#). Any further distribution of this work must maintain attribution to the author(s) and the title of the work, journal citation and DOI.

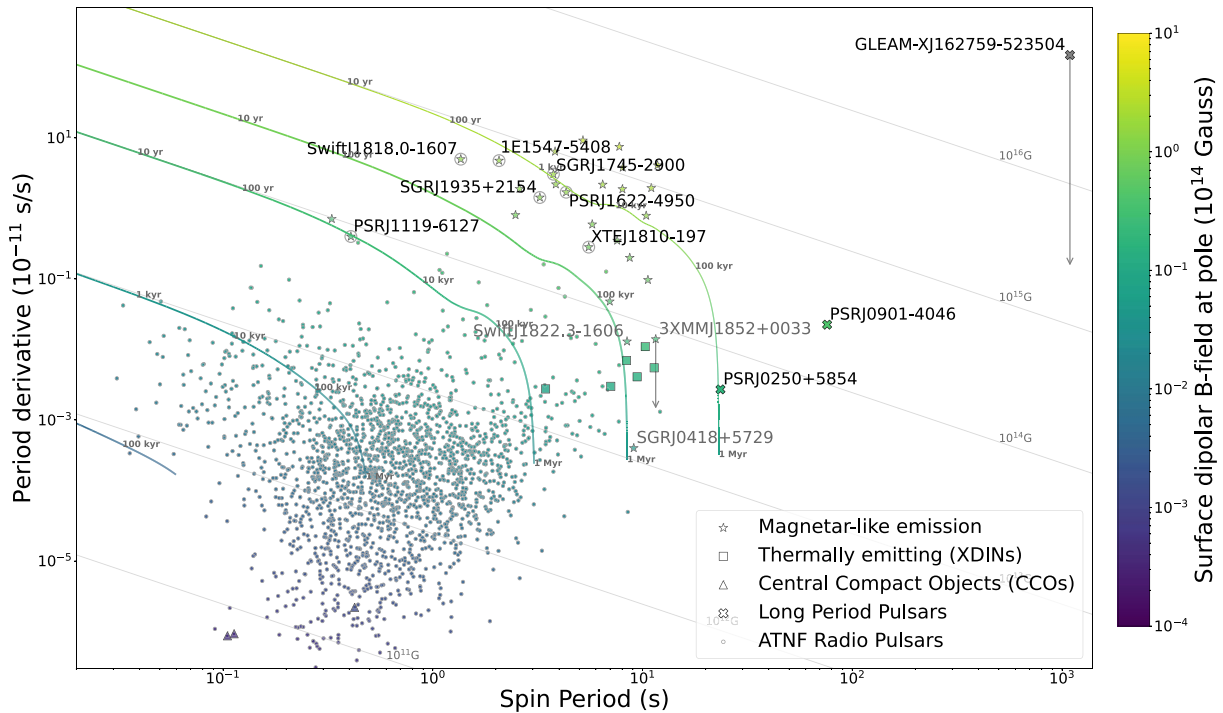


Figure 1. $P-\dot{P}$ diagram for different neutron star classes. The names are shown for radio magnetars (also displayed with a gray circle), low-field magnetars, and long-period pulsars (including GLEAM-X J1627). Light gray lines correspond to constant magnetic fields, while the colored curves assumed magnetic field decay in the crust (see Section 4 for details). Colors refer to the surface dipolar magnetic field strength at the pole.

stars rather than canonical pulsar radio emission (Geng et al. 2016).

A peculiar radio transient with a periodicity of ~ 1091 s (GLEAM-X J162759.5-523504.3; hereafter GLEAM-X J1627) was discovered in archival data taken by the Murchison Widefield Array (MWA; Tingay et al. 2013; Wayth et al. 2018). This source was found to be active during 2018 January–March with 5–40 Jy bright radio pulses lasting about 10–30 s and repeating with an 18 min periodicity (Hurley-Walker et al. 2022). The bright pulses have a linear polarization degree of $88\% \pm 1\%$ and a dispersion measure $DM = 57 \pm 1$ pc cm $^{-3}$, the latter resulting in a distance of 1.3 ± 0.5 kpc according to the Galactic electron-density model by Yao et al. (2017). The observed radio luminosity and emission timescales pointed to a coherent emission process. On the one hand, the long spin period could be explained by a rotating magnetic white dwarf emitting as a pulsar-like dipole. On the other hand, the source radio properties resembled those of radio magnetars. In any of the abovementioned cases, the nature of this source would be quite extreme within these source classes (Hurley-Walker et al. 2022). In this work we report on X-ray observations of GLEAM-X J1627 performed with the Chandra X-ray Observatory on 2022 January 22–23 (Section 2.1) and simultaneous radio observations using MWA, MeerKAT, and the Australia Telescope Compact Array (ATCA; Section 2.2). We also report on optical and near-infrared (NIR) data sets collected in European Southern Observatory (ESO) public survey projects and in the DECam Plane Survey, as well as optical data acquired in recent Southern African Large Telescope (SALT) observations (Section 2.3). We use these observations to constrain the nature of this periodic radio transient both in the neutron star and white dwarf scenarios. We report the results in Section 3 and discuss them in Section 4. Conclusions follow in Section 5.

2. Observations and Data Analysis

2.1. X-Ray Observations: Chandra

The Chandra X-ray Observatory observed GLEAM-X J1627 twice using the Advanced CCD Imaging Spectrometer (ACIS; Garmire et al. 2003) instrument, from 2022 January 22 at 20:51:32 to January 23 at 03:05:43 TT (ObsID: 26228), and then again on 2022 January 23 from 06:04:47 to 09:26:34 TT (ObsID: 26282). All observations were performed in timed exposure (TE) imaging mode with Very Faint (VF) telemetry format. The source was positioned on the back-illuminated ACIS-S3 CCD at the nominal target position (R.A. = $16^{\text{h}}27^{\text{m}}59^{\text{s}}.5$, decl. = $-52^{\circ}35'04''.3$; J2000.0; uncertainty of $2''$; Hurley-Walker et al. 2022).

Standard processing of the data was performed by the Chandra X-ray Center to Level 1 and Level 2 (processing software DS 10.10.2.1). The data were reprocessed using the CIAO software (version 4.14; CALDB 4.9.6). We used the latest ACIS gain map, and applied the time-dependent gain and charge transfer inefficiency corrections. The data were then filtered for bad event grades and only good time intervals were used. No high-background events were detected, resulting in an exposure time of about 20.1 and 10.1 ks for the first and second observation, respectively.

We did not detect any significant X-ray emission at the radio position of GLEAM-X J1627 when coadding the two Chandra observations (total on-source live time of 29.8 ks). Specifically, we detected only one photon in the 0.3–8 keV energy range within a $2''$ error circle centered on the source position. Taking a 3σ upper limit of 8.9 photons (Gehrels 1986), we can infer an upper limit on the X-ray quiescent count rate of GLEAM-X J1627 of $\sim 2.9 \times 10^{-4}$ counts s $^{-1}$ (at 3σ c.l.). We checked this number using different approaches. We extracted source counts from circular regions with a radius of $0''.8$ (enclosing

Table 1
X-Ray and Radio Observations

Instrument	Start Time (UTC) (YYYY Mmm DD hh:mm:ss)	End Time (UTC)	Exposure ^a (ks)	Obs. ID	Mode ^b
Chandra	2022 Jan 22 20:50:23	2022 Jan 23 03:04:34	19.82	26228	TE VF (3.041 s)
Chandra	2022 Jan 23 06:03:38	2022 Jan 23 09:25:25	9.98	26282	TE VF (3.141 s)
Instrument	Start Time (UTC) (YYYY Mmm DD hh:mm:ss)	End Time (UTC)	Integration time ^c (min)	Observing Band (GHz)	3 σ limit (μ Jy beam ⁻¹)
MWA	2022 Jan 21 23:45:58	2022 Jan 22 01:24:38	111	0.17–0.2	...
MWA	2022 Jan 22 23:45:58	2022 Jan 23 01:24:38	111	0.17–0.2	5000
MeerKAT	2022 Jan 23 03:32:49	2022 Jan 23 05:12:48	70	0.58–1.1	84
ATCA	2022 Jan 22 15:00:18	2022 Jan 22 19:41:42	252	4–6	72
ATCA	2022 Jan 22 15:00:18	2022 Jan 22 19:41:42	252	8–10	60

Notes.

^a Deadtime corrected on-source time.

^b TE: timed exposure; VF: very faint telemetry format. The temporal resolution is given in parentheses.

^c On-source only; not including time spent on calibrators.

90% of the point-spread function, PSF, region at 1 keV), 2", or 3". For the background, we also assumed different extraction regions: an annulus with an inner radius equal to the source radius and an outer radius 5 times larger, or circles of the same size as the source extraction regions, far from the aim point but located on the same CCD. We used the CIAO SRCFLUX tool to extract the upper limits of the source count rate using all the different combinations of source and background extractions. In all cases, the tool gives a 3 σ limit on the background-subtracted count rate at the position of the radio source of 3×10^{-4} counts s⁻¹ (0.3–8 keV) after merging the event files from the two observations.

2.2. Radio Observations: MWA, MeerKAT, and ATCA

We performed near-contemporaneous radio observations with three different radio telescopes: the MWA, MeerKAT, and ATCA, spanning a frequency range of 170 MHz–9 GHz. We found no pulsed or continuum radio emission at the location of GLEAM-X J1627. The observation properties and the derived (3 σ) upper limits of the flux density are shown in Table 1.

2.2.1. MWA Observations

We observed with the Phase II extended configuration of the MWA using 5 min pointed snapshots at 170–200 MHz as GLEAM-X J1627 transited (i.e., when the primary beam sensitivity was highest). One-hundred and four tiles were functional at the time of observing. We reduced the data using the download, calibration, and imaging stages of the GLEAM-X pipeline⁹ (Hurley-Walker et al. 2022). Stokes *I* imaging was performed with WSCLEAN (Offringa et al. 2014) using standard GLEAM-X settings, resulting in a restoring beam size of 1'. Primary beam correction was performed using the most up-to-date MWA beam model (Sokolowski et al. 2017). At these frequencies, the source dispersion measure of 57 pc cm⁻³ causes ~ 2 s of smearing across the band, so there is no need to perform de-dispersion to make a detection. Since the pulse profile of GLEAM-X J1627 was previously 30–60 s wide, and the integration time is 4 s, we split the data into 32 s intervals and folded at $P = 1091$ s. No pulsed emission was

observed to a 3 σ limit of 16 mJy beam⁻¹ per (32 s long) phase bin. No bright single pulses were observed in any individual time step, down to a 3 σ upper limit of 100 mJy beam⁻¹. The rms noise σ in each 5 min snapshot is 10 mJy beam⁻¹. By stacking all 222 minutes of observing time, we obtained a 3 σ upper limit in the mosaic of 5 mJy beam⁻¹.

2.2.2. MeerKAT Observations

We used MeerKAT in the UHF band (580 MHz–1.1 GHz) with 8 s time integration. Calibration was provided by the Science Data Processor pipeline at the South African Radio Astronomy Observatory. Dispersion smearing was just 0.5 s, less than the integration interval. We used WSCLEAN to image the calibrated measurement set, selecting only baselines with lengths $>573 \lambda$, so as to down-weight contaminating Galactic diffuse emission on scales of $>0^\circ.1$. We imaged 9 sq. deg. with a pixel scale of 1"8, at a ‘‘Briggs’’ robust weighting of 0.0 (Briggs 1995), outputting 10 equally spaced channels and cleaned them jointly to account for spectral variations across the wide bandwidth due to intrinsic source spectra and the primary beam. We CLEANed down to 3 \times the rms of the residuals, and then down to 1 \times the rms for pixels within regions already selected as containing CLEAN components (`-auto-mask=3`; `-auto-threshold=1`). We imaged each 8 s correlator dump with the continuum sources subtracted and detected no single pulses to a 3 σ limit of 3 mJy beam⁻¹. Splitting the data into 32 s intervals and folding at $P = 1091$ s, no pulsed emission was observed, to a 3 σ limit of 300 μ Jy beam⁻¹ per phase bin. The rms of the time-integrated image is 28 μ Jy beam⁻¹. Therefore, we obtained a 3 σ upper limit on a persistent radio source of 84 μ Jy beam⁻¹.

2.2.3. ATCA Observations

We observed with ATCA simultaneously in the *C* (4–6 GHz) and *X* (8–10 GHz) bands using the Compact Array Broadband Backend (Wilson et al. 2011). We applied primary (bandpass and absolute flux density scale) calibration solutions derived from PKS 1934-638 and secondary (gain) calibration solutions from PKS 1646–50. Imaging was performed in MIRIAD (Sault et al. 1995). The rms in the *C*- and *X*-band images was 24 and 20 μ Jy beam⁻¹, leading to 3 σ upper limits of 72 and

⁹ <https://github.com/tjgalvin/GLEAM-X-pipeline>

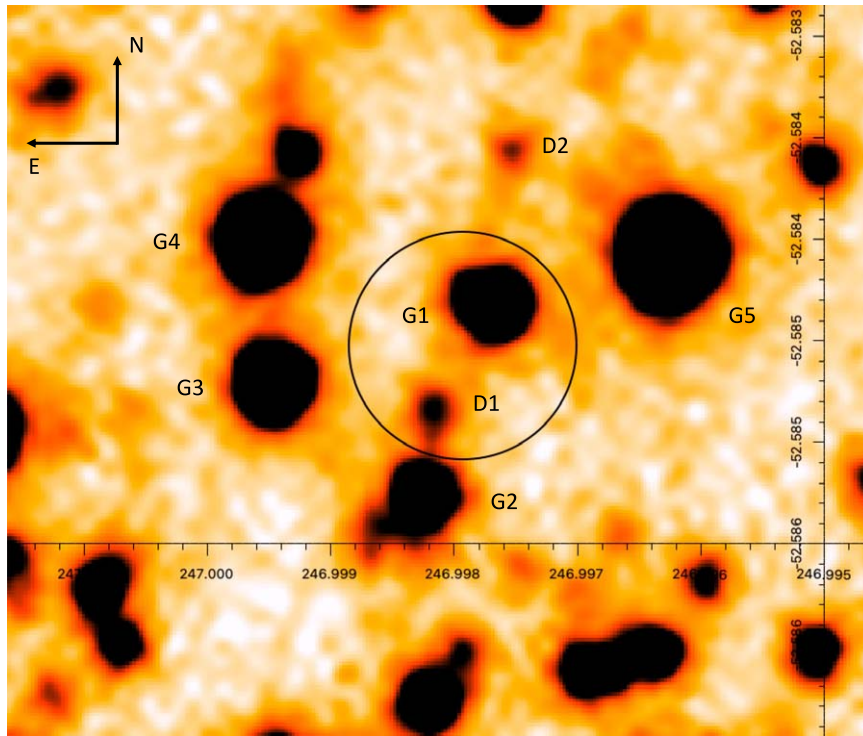


Figure 2. The z -band DECAPS image of the field of GLEAM-X J1627. The position of the radio source and its 1σ error circle (with a radius of $2''$) are reported. The positions of the five Gaia (G1, G2, G3, G4, G5) and two DECAPS (D1, D2) objects within $4''$ are also reported. North is up and east is left.

$60 \mu\text{Jy beam}^{-1}$, respectively. Folding the data resulted in a relatively poor 3σ upper limit of 5 mJy beam^{-1} due to the imperfect (u, v) coverage.

2.3. Optical and NIR Observations

2.3.1. Archival Imaging Observations

The field of GLEAM-X J1627 has been observed in the optical band by the VST Photometric $H\alpha$ Survey of the Southern Galactic Plane and Bulge (VPHAS+; Drew et al. 2014). The public VPHAS+ Data Release 4 contains several images of the field of GLEAM-X J1627 acquired between 2016 and 2017 with the OmegaCAM imager mounted on the 2.6 m VLT Survey Telescope (VST) in the u , g , r and i filters (six, nine, 12, and six images, respectively) and narrowband NB_659 filter centered on $H\alpha$ (nine images). The single exposures were 150 s for the u filter, 40 s for the g filter, 25 s for the r and i filters, and 120 s for the $H\alpha$ filter. The calibrated images and derived source catalogs were retrieved from the ESO archive.¹⁰

The field has also been covered in the optical band by the DECam Plane Survey (DECAPS; Schlafly et al. 2018) with the DECam imager mounted at the Víctor M. Blanco 4 m Telescope in Chile between 2016 March and 2017 May (see Figure 2). Observations were performed using five broadband filters: g , r , i , z , and Y . The single exposures were 96 s for the g filter and 30 s for the other filters, reaching much deeper limits than VPHAS+ (see Table 2). The calibrated images and derived multiband merged photometry catalogs were retrieved from the DECAPS archive.¹¹

The field has been covered in the NIR by the Vista Variables in the Via Lactea eXtended ESO Public Survey (VVVX; Minniti et al. 2010). About 200 images were acquired in the J , H , and K_s filters using the 4 m Visible and Infrared Survey Telescope for Astronomy (VISTA) between 2016 July and 2019 September, with single exposures of 10 s for the J filter, 6 s for the H filter, and 4 s for the K_s filter adopting different ditherings. The calibrated stacked images and derived catalogs were retrieved from the ESO archive.

We also inspected the Gaia early and final third data releases (EDR3, DR3; Gaia Collaboration et al. 2021; Babusiaux et al. 2022) to search for a possible optical counterpart within the $2''$ of the radio position of GLEAM-X J1627 (1σ confidence; Hurley-Walker et al. 2022) and found one faint ($m_G = 20.24$, $B_p = 21.22$, $R_p = 19.37$) source, here named G1. There are four additional bright Gaia objects nearby, which we name G2, G3, G4, and G5 (see Table 2 for more details). Unfortunately, the parallaxes of these faint Gaia stars are undetermined, preventing a comparison with the radio-derived distance of 1.3 ± 0.5 kpc of GLEAM-X J1627 (Babusiaux et al. 2022). The positions of GLEAM-X J1627, the Gaia stars, and the two other fainter stars detected in the DECAPS survey are displayed on a z -band DECAPS cutout image in Figure 2. In Table 2 we report the magnitudes of these stars, and to keep uniformity we have used the AB-to-Vega conversion of Fukugita et al. (1996) for the g , r , i , and z bands and Hewett et al. (2006) for the Y band.

We searched for optical and NIR sources close to the position of GLEAM-X J1627 in the VPHAS+, DECAPS, and VVVX catalogs. None of the Gaia stars is detected in the VPHAS+ u band and G2 and G3 are not detected in the VPHAS+ g band. Table 2 reports the derived optical (g , r , i , and $H\alpha$) magnitudes of these Gaia objects following the prescription for VPHAS+ data releases. Namely, we used the

¹⁰ <http://archive.eso.org>

¹¹ <http://decaps.skymaps.info/>

Table 2

Magnitudes of the Five Gaia Sources and the Two Faint Optical Sources within $4''$ from the Position of GLEAM-X J1627 as Derived from the VPHAS+, DECAPS, and VVVX Public Surveys, as well as from Recent Observations at SALT. Magnitudes are in Vega system.

Gaia											
Source	R.A. (J2015.5)	Decl. (J2015.5)	$d_{\text{GLEAM}} (")$	m_G	B_p	R_p					
G1	16 ^h 27 ^m 59 ^s .434	-52°35' 03 ''58	0.9	20.24	21.22	19.37					
G2	16 ^h 27 ^m 59 ^s .579	-52°35' 06 ''96	2.8	20.60	21.72	19.43					
G3	16 ^h 27 ^m 59 ^s .870	-52°35' 04 ''98	3.4	20.31	22.02	19.34					
G4	16 ^h 27 ^m 59 ^s .097	-52°35' 02 ''71	4.0	18.81	20.04	17.84					
G5	16 ^h 27 ^m 59 ^s .891	-52°35' 02 ''44	4.0	19.52	20.57	18.48					
VPHAS+ survey											
Source				g	r	i	$H\alpha$				
G1				21.98(11)	20.30(8)	19.61(8)	20.23(14)				
G2				...	21.11(13)	20.01(11)	20.65(20)				
G3				...	21.08(13)	19.74(9)	20.54(18)				
G4				20.70(5)	18.92(5)	17.97(3)	18.81(5)				
G5				21.49(8)	19.64(6)	18.75(4)	19.55(8)				
DECAPS and VVVX surveys											
Source	R.A. (J2000)	Decl. (J2000)	$d_{\text{GLEAM}} (")$	g	r	i	z	Y	J	H	K_s
G1	16 ^h 27 ^m 59 ^s .45	-52°35' 03 ''5	0.9	21.731(15)	19.906(10)	20.226(11)	19.250(11)	18.256(12)	17.733(28)	17.088 (42)	16.784 (71)
G2	16 ^h 27 ^m 59 ^s .58	-52°35' 07 ''0	2.8	22.432(26)	20.434(15)	19.514(11)	18.942(10)	18.535(17)	17.947(24)	17.542 (62)	17.109 (90)
G3	16 ^h 27 ^m 59 ^s .87	-52°35' 05 ''0	3.4	22.978(45)	20.361(14)	19.047(8)	18.126(7)	17.744(9)	16.870(10)	15.989 (14)	15.757 (24)
G4	16 ^h 27 ^m 59 ^s .10	-52°35' 02 ''7	4.0	20.567(8)	18.649(6)	17.705(6)	17.035(6)	16.750(6)	16.126(7)	15.517 (11)	15.311 (20)
G5	16 ^h 27 ^m 59 ^s .89	-52°35' 02 ''4	4.0	21.221(10)	19.297(8)	18.359(6)	17.677(6)	17.398(8)	16.764(9)	16.185 (19)	15.937 (28)
D1	16 ^h 27 ^m 59 ^s .56	-52°35' 05 ''5	1.4	...	22.664(19)	21.393(41)	20.453(32)	20.056(51)	19.146(63)	18.312 (109)	18.152 (205)
D2	16 ^h 27 ^m 59 ^s .40	-52°35' 00 ''9	3.7	...	22.625(18)	21.671(52)	20.777(42)	20.500(75)
SALT											
Source label				r'	i'	z'					
G1				20.05(3)	19.21(2)	18.64(3)					
G2				21.11(8)	19.54(4)	18.90(5)					
G3				20.32(4)	19.14(2)	18.25(2)					
G4				18.75(1)	17.85(1)	17.21(1)					
G5				19.40(2)	18.48(1)	17.84(2)					
VPHAS+ 5σ Upper limits											
$u = 21.6$ $g = 22.8$ $r = 21.6$ $i = 20.4$ $H\alpha = 20.7$											
DECAPS 5σ and VVVX 3σ Upper limits											
$g = 23.7$ $r = 22.9$ $i = 22.8$ $z = 22.5$ $Y = 21.6$ $J = 19.9$ $H = 19.0$ $K_s = 18.2$											

Note. Magnitudes are in the Vega system.

fluxes derived with an optimal aperture radius of $1''$ (Aperture 3), applied aperture, air mass, and exposure time correction and adopted the zero points in the Vega system reported in the

corresponding image catalogs. On the other hand, all the Gaia objects are detected in the DECAPS survey. This survey reaches much fainter magnitude limits (see Table 2), allowing

us to identify two additional faint sources in the r , i , z , and Y filters. These two sources, named D1 and D2, are located at an angular distance of $1''.4$ and $3''.7$ from GLEAM-X J1627, respectively (see Figure 2). Given the large uncertainties in the VPHAS+ photometry, we henceforth use the DECAPS photometry to derive information on the nature of the seven detected sources.

Furthermore, while the same procedure used for VPHAS+ has been adopted to the VISTA image catalogs, the two faint sources, D1 and D2, are not detected in the single images. We then used the NIR PSF photometry recently performed for the VVV survey (Alonso-García et al. 2018) and in particular for the VVVX survey (J. Alonso-García et al. 2022, in preparation) for the sky region of GLEAM-X J1627. The latter is obtained by stacking all images, making it possible to reach much fainter magnitudes in the J , H , and K_s bands (see Table 2).

2.3.2. SALT Observations

The field of GLEAM-X J1627 was observed on 2022 April 27 at the 10 m SALT (Buckley et al. 2006) equipped with SALTICAM (O’Donoghue et al. 2006) in r' and i' Sloan Digital Sky Survey (SDSS) filters, and with the Robert Stobie Spectrograph (RSS; Burgh et al. 2003) in imaging mode with the z' SDSS filter. Three images for each filter were acquired with exposure times of 120 s (r' and i' filters) and 150 s (z' filter). The r' - and i' -band acquisitions were performed cyclically (r' , i' , r' , i' , etc.) from 21:37:03 to 21:56:08 UT, while z' -band exposures were acquired sequentially from 21:24:10 to 21:29:51 UT. A 2×2 binning and Faint/Slow mode were adopted for these observations.

Images have been processed with the `Pysalt` pipeline, which corrects for bias, crosstalk, gain, and amplifier mosaicking. No standard stars were observed and hence no absolute flux calibration was performed due to the moving pupil of the telescope (see Buckley et al. 2008). Therefore, the images were analyzed to obtain differential photometry with the bright Two Micron All Sky Survey (2MASS) stars 2MASS J16275876–5235170, 2MASS J16280154–5235061, and 2MASS J16275821–5234474, which have stable photometric measurements in DECAPS.

Aperture photometry was performed on each image and on stacked images using the three exposures in each band with the `iraf` task `daophot`. The targets detected in these images are the five Gaia stars but not the two faint ones found in DECAPS. The differential instrumental magnitudes were then converted into r -, i -, and z -filter magnitudes using the DECAPS magnitudes of the bright stars. Since the Gaia stars do not show variability within their photometric uncertainties, in Table 2 we report their magnitudes obtained from the stacked images. The associated uncertainties are statistical only. The results of the photometry of the Gaia stars appear consistent to be with the magnitudes obtained from DECAPS. The lack of detection of the two faint DECAPS sources is due to a shallower limiting magnitude.

Two low-resolution spectra, with a 30 min exposure each, were acquired with the RSS mounted on SALT in long-slit mode. The first spectrum was taken starting on 2022 February 11 at 02:35:49 UT, with the second one starting on 2022 February 12 at 02:12:42 UT. The PG0300 (300 l mm^{-1}) grating was used with a tilt angle of $5^\circ.75$, yielding a usable wavelength range of $\sim 3900\text{--}9000 \text{ \AA}$ and a resolving power of $R \simeq 600$ at 5000 \AA . We used the $1''.5 \times 8'$ long slit placed at a position

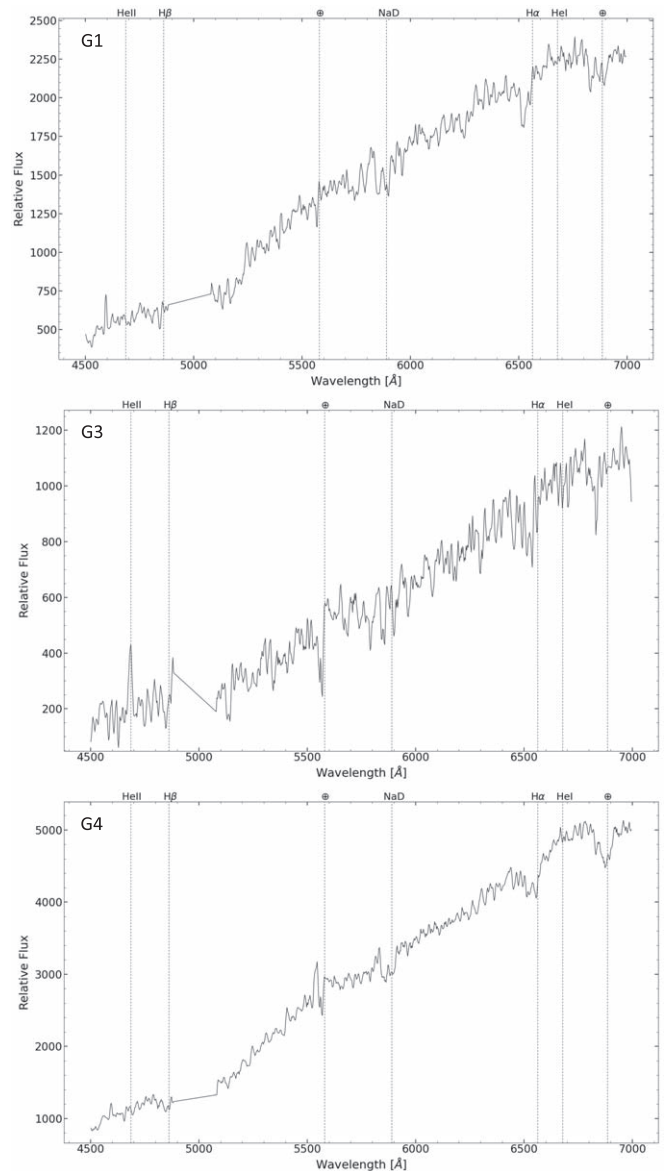


Figure 3. From top to bottom: the combined average SALT spectra of G1, G3, and G4 in the range 4500–7000 Å showing absorption features typical of mid/late-type stars. The vertical lines report expected hydrogen Balmer ($H\alpha$ and $H\beta$) and helium lines ($He I$ and $He II$). Telluric features are also marked using an circled cross. The gap around 5000 Å is due to the mosaicked chips of the RSS detector. A residual artifact is present in the spectrum of G3 around the $He II$ line.

angle of $PA = 290^\circ$ (measured from north to east) for both observations to pass through stars G1, G3, and G4 (see Figure 3). The spectra were reduced using standard `iraf` tasks including flat-field, background subtraction, and cosmic-ray removal. The wavelength calibration was performed using an argon arc lamp. No standard stars were observed, and thus the spectra were not calibrated in flux.

3. Results

3.1. X-Ray and Radio

Using the HEASARC PIMMS tool, we estimated the 3σ upper limit on the source X-ray flux assuming different spectral models. The expected absorption column density N_H from the N_H –DM relation by He et al. (2013) is $N_H \simeq 2 \times 10^{21} \text{ cm}^{-2}$

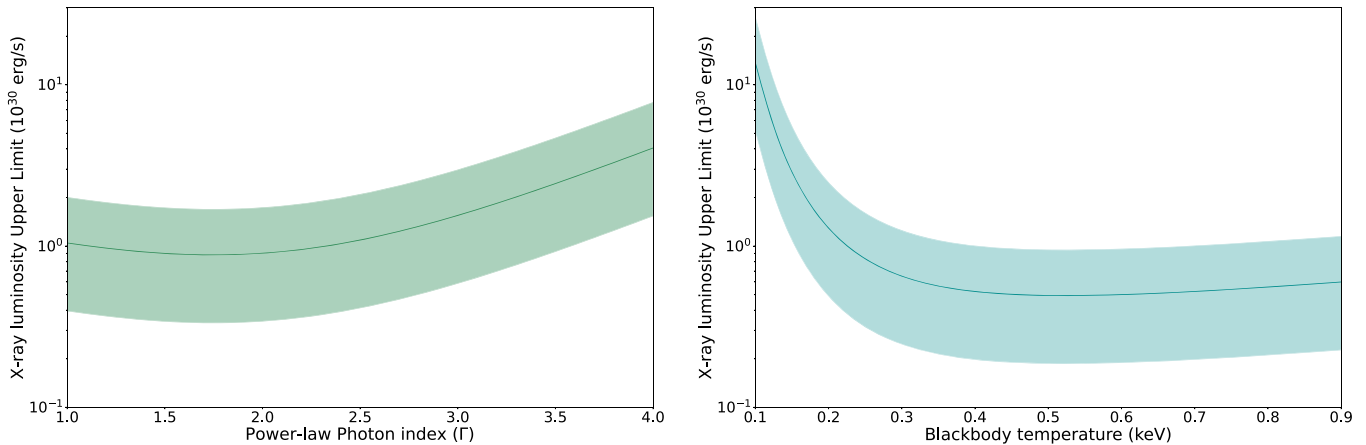


Figure 4. Upper limits at 3σ confidence level on the X-ray luminosity of GLEAM-X J1627 derived assuming either an absorbed power-law spectrum with $\Gamma = 1-4$ (left panel) or an absorbed blackbody spectrum with $kT = 0.1-0.9$ keV (right panel). The solid curves mark the limits derived assuming a distance of 1.3 kpc, while the shaded areas indicate the range of luminosities that account for the uncertainty in the source distance.

using a $DM = 57 \text{ pc cm}^{-3}$. We derived an upper limit on the 0.3–10 keV absorbed (unabsorbed) flux of $3.1(4.5) \times 10^{-15} \text{ erg cm}^{-2} \text{ s}^{-1}$ and $2.0(3.2) \times 10^{-15} \text{ erg cm}^{-2} \text{ s}^{-1}$ (3σ c.l.) for a power law with $\Gamma = 2$ and a blackbody with $kT = 0.3$ keV, respectively. Assuming that the source is at a distance of 1.3 kpc (as derived from its DM), these values translate into a luminosity limit of $9.1 \times 10^{29} \text{ erg s}^{-1}$ for a power-law spectrum and $6.5 \times 10^{29} \text{ erg s}^{-1}$ for a blackbody spectrum. To take into account the uncertainties related to the assumed spectral model, we make the same estimates as above but assume an absorbed power-law spectrum with a photon index ranging from $\Gamma = 1-4$, as expected for rotation-powered pulsars, and an absorbed thermal spectrum modeled by a blackbody with temperature between $kT = 0.1-0.9$ keV, typical of a magnetar in quiescence (Rea & Esposito 2011; Coti Zelati et al. 2018). In Figure 4 we plot our upper limits as a function of the different assumed spectral shapes, accounting also for the uncertainty on the distance (1.3 ± 0.5 kpc).

The 3σ upper limits on the radio flux density at our observed frequencies are given in the final column of Table 1, with a strong limit of $\lesssim 100 \mu\text{Jy beam}^{-1}$ at gigahertz frequencies.

3.2. Optical and NIR

Figure 3 shows the optical spectra of G1, G3, and G4. These spectra do not reveal emission lines that could point to an interacting binary or to the presence of deep absorption features from a hot companion star, such as a white dwarf. Note that a sky artifact is present at He II for the G3 star. The SALT spectra were compared with the stellar spectral library of Jacoby et al. (1984), which first suggest a spectral type around mid/late-G star for G1, a late-G or early-K star for G3, and a late-F or early/mid-G star for G4. The low resolution of the spectra does not allow us to better constrain the nature of these stars. In aid of these, we have compared the observed VPHAS+ and DECAPS ($g-r$, $r-i$) colors with the VST/OmegaCAM synthetic colors for main-sequence stars tabulated in Drew et al. (2014) for extinctions, A_V , from 0 to 8 in steps of 2 and adopting the mean Galactic reddening law $R_V = 3.1$. The total extinction in the direction of the source is estimated to be $A_V = 4.15$ (Schlafly & Finkbeiner 2011). However, the observed colors do not match a single sequence, indicating that these stars suffer different extinctions likely due to different distances. The same is true for the NIR ($J-H$,

$H-K$) colors when compared to the main-sequence stars in the 2MASS J , H , and K_s bands by Straizys & Lazauskaitė (2009) applying extinctions ranging from $A_V = 0, 2$, and 4 and using the VISTA calibration from 2MASS (González-Fernández et al. 2018). Given the deeper and more accurate DECAPS photometry and the PSF VISTA NIR photometric measurements, we extracted the spectral energy distributions (SEDs) for each of the seven stars applying an extinction correction from $A_V 2$ to 4.

Figure 5 reports the SEDs for these objects together with the best-fitting blackbody functions for each extinction correction. The SEDs are constructed with few measurements, giving a low quality of the fits (χ_{red}^2 ranging from 5 to 10). Given the unknown distance, and thus reddening, and relying on the optical spectra acquired for G1, G3, and G4, we tentatively ascribe for G1 an A_V between 2 and 2.7 with a temperature in the range 4800–5600 K and thus a mid G to early K spectral type; for G3, an $A_V \sim 4$ with a temperature ~ 4300 K, and thus a mid K spectral type, slightly later than estimated from spectra, or otherwise a higher reddening $A_V \sim 4.2$ to match a late G or early K type; and for G4 an A_V that should be between ~ 3 and 3.8 with a temperature $\sim 5500-6300$ K to match the late F or mid G spectral type. For G2 we do not have spectra to constrain the spectral type and thus the extinction, A_V , could be between 2 and 4. This gives a wide range of temperatures, $\sim 4400-8300$ K, which correspond to spectral types ranging from mid or late A to mid K. The case of G5 is similar. Therefore, for A_V between 2 and 4, the temperature would result in the range of 4300–8000 K spanning spectral types between late A to mid K. Also, for D1 and D2, an extinction A_V between 2 and 4 would result in blackbody temperatures in the range 3000–4800 K and 3400–7300 K, respectively. The spectral types of these two faint objects, if they are main-sequence stars, would range from mid M to early K and from mid M to early F, respectively.

4. Discussion

In this work, we have presented simultaneous X-ray and radio observations of the 18 min radio transient GLEAM-X J1627, and deep optical and NIR observations of the field.

We have derived the deepest X-ray upper limits on its emission, an important ingredient in constraining its nature. The exact X-ray luminosity limit strongly depends on the

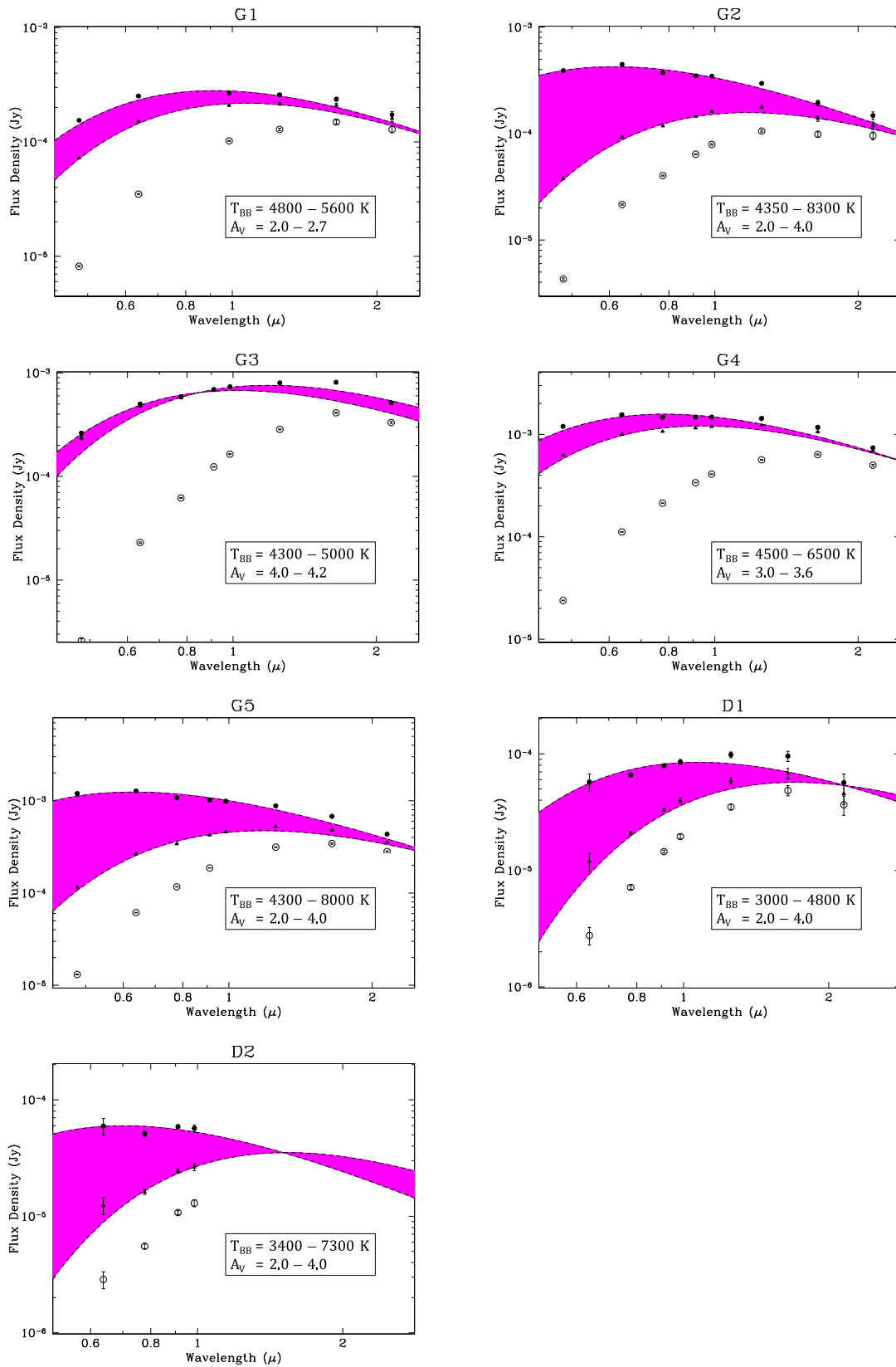


Figure 5. From left to right, top to bottom: SEDs of G1, G2, G3, G4, G5, D1, and D2 adopting different extinction corrections, shown with their best-fitting blackbody models. The open circles report the SEDs without reddening corrections, while the filled triangles and circles report the SEDs corrected for the low and high values of extinctions, A_V , respectively, as reported in the text (see also Section 3.2). The shaded magenta areas comprise the range of blackbody temperatures and extinctions.

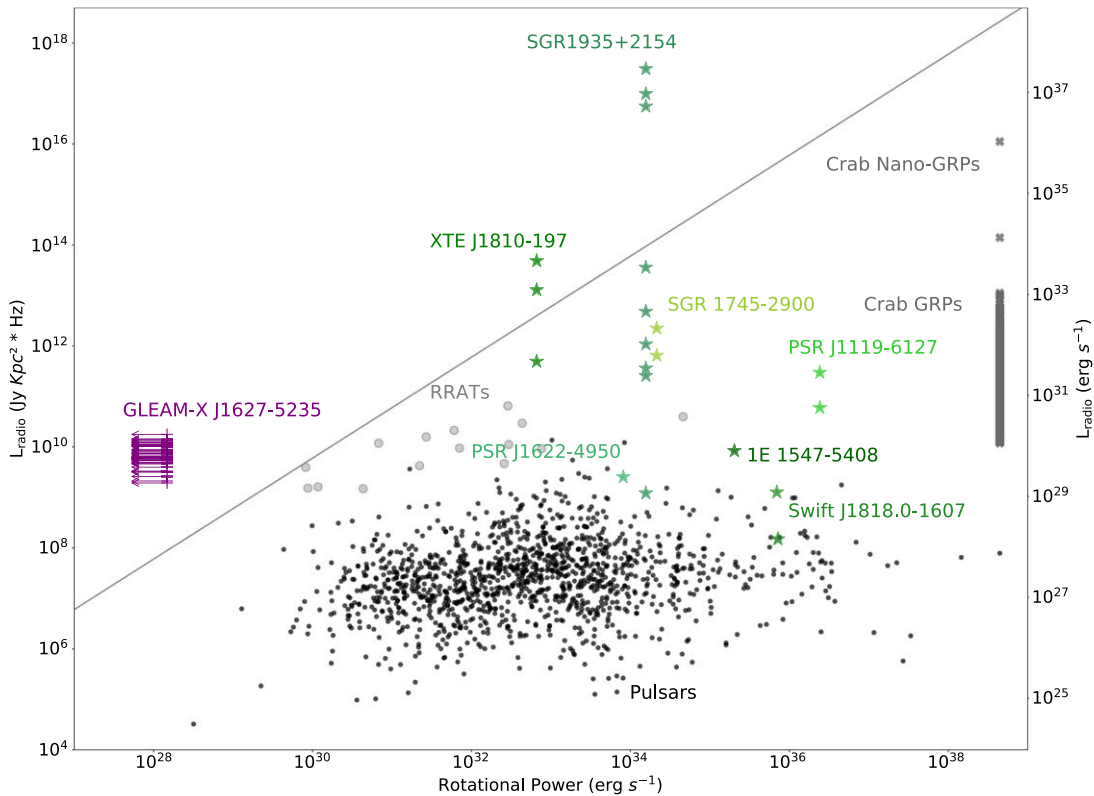


Figure 6. Radio luminosity vs. rotational power of bright single-peak emission for all pulsar classes and the GLEAM-X J1627’s upper limits. Radio magnetars’ bright single pulses are labeled in green. The gray solid line marks the relation $L_{\text{radio}} = \dot{E}_{\text{rot}}$.

assumed spectral shape and distance: we hereafter assume $L_X \leq 10^{30} \text{ erg s}^{-1}$ as an average value over the different spectral models and distance errors (see Figure 4 for the exact calculations). The radio limit in quiescence we have derived from the MeerKAT observations, assuming isotropic emission and a flat spectrum in the observing radio band, resulted in a quiescent radio luminosity limit of $L_{\text{radio}} \leq 10^{25} \text{ erg s}^{-1}$. This radio limit is very low but not unusual in the pulsar population (see also Figure 6). We note that these limits are derived under strong assumptions, which may not necessarily be correct but are only presented to give an idea of the order of magnitude.

Furthermore, the optical and NIR observations of the field revealed several objects potentially compatible with the source position (see Figure 2), which we discuss in the following subsections.

4.1. The Transient Periodic Radio Emission in the Framework of Radio Magnetars

The observed radio characteristics of GLEAM-X J1627, namely its transient radio emission, its bright and variable single peaks, the pulse profile variability, and its high linear radio polarization (Hurley-Walker et al. 2022), are perfectly in line with what is typically observed for radio-loud magnetars. In fact, radio emission in magnetars is typically observed in coincidence with their X-ray outbursts, and with large variability in terms of luminosity and shape of their single peaks (see Esposito et al. 2021 for a recent review, and references therein). The nondetection of an X-ray outburst at the time of GLEAM-X J1627’s radio activation is not surprising, since it might have been easily missed due to the sparse and shallow coverage of the large-field-of-view X-ray monitors. The only apparent inconsistency between GLEAM-X J1627 and

the population of radio-loud magnetars is thus far its 18 min periodicity (see Figure 1).

However, as extensively studied by Ronchi et al. (2022), the 18 min periodicity of GLEAM-X J1627’s radio emission cannot be reconciled with the pulsar scenario when only dipolar losses and a typical crust+core field configuration are considered. This would require the assumption that this pulsar has an unreasonably large magnetic field ($B \sim 10^{16} - 10^{17} \text{ G}$) that does not decay in time (something unseen in the pulsar population; see also Figure 1 by Ronchi et al. 2022). In a typical crust+core field configuration, the magnetic field is expected to decay on a timescale of 10–100 Kyr depending on its intensity (the stronger the field, the faster it decays; see the spin-period evolutionary curves in Figure 1).

A more plausible possibility is that fall-back accretion from the supernova could easily have slowed a magnetar with a magnetic field of $\sim 10^{13} - 10^{14} \text{ G}$ down to its current period of 18 min in $\sim 10^4 - 10^6 \text{ yr}$. In this scenario, the supernova fossil-disk is now inactive (because the disk is now too cold or has been completely disrupted), so the source had resumed its dipolar-driven rotation and normal radio-loud magnetar activity. However, its spin period has been driven at a longer value than that of its peers at the same age and field ($\sim 10^{14} - 10^{15} \text{ G}$; for detailed simulations, see Ronchi et al. 2022; Gençali et al. 2022, and Tong 2022).

Several studies have discussed the radio luminosity of GLEAM-X J1627 during its radio outburst in comparison with the limits of its rotational energy (Erkut 2022; Hurley-Walker et al. 2022). In particular, assuming isotropic emission, the radio luminosity of the brightest single peaks ($L_{\text{radio}} \sim 10^{30} - 10^{31} \text{ erg s}^{-1}$; Hurley-Walker et al. 2022) exceeds the limits on the rotational power of the source by a few orders of magnitude. Figure 6 shows those peak radio luminosities and the rotational power of GLEAM-X J1627 in

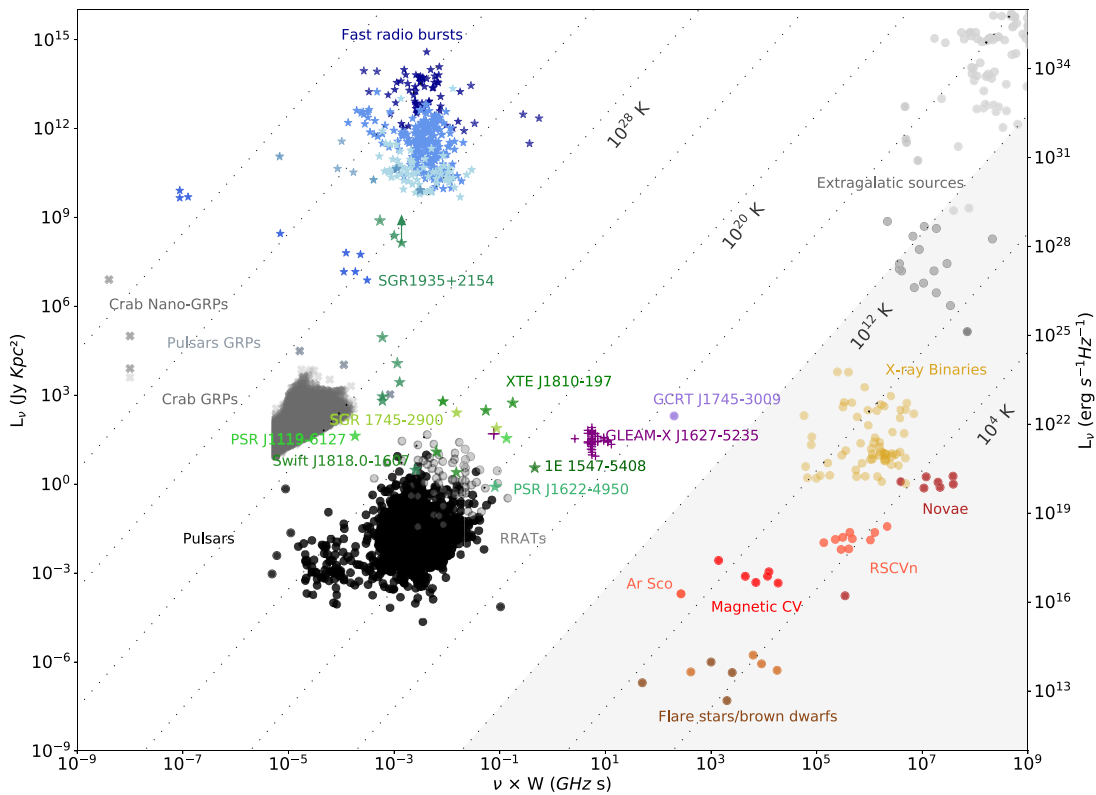


Figure 7. Radio-transient plane including all transient sources with a particular focus on radio magnetars’ bright single pulses (different green tones), GLEAM-X J1627 (violet), and white dwarf systems (different red tones). Data collected from Camilo et al. (2006, 2007), Weltevrede et al. (2011), Deller et al. (2012), Lynch et al. (2015), Majid et al. (2017), Pearlman et al. (2018), Lower et al. (2020), Esposito et al. (2021), Pietka et al. (2015), Marsh et al. (2016), Keane (2018), and Nimmo et al. (2022).

comparison with other pulsars, rotating radio transients (RRATs) and radio-loud magnetars. For the radio-loud magnetars, given their large variability, we have chosen the brightest radio pulses reported in the literature (data collected from Camilo et al. 2006, 2007; Weltevrede et al. 2011; Deller et al. 2012; Lynch et al. 2015; Majid et al. 2017; Pearlman et al. 2018; Lower et al. 2020, and Esposito et al. 2021). It is well known that assuming isotropic radio emission is not realistic, and a beaming factor necessarily has to be present (see, e.g., Erkut 2022). However, the relation between the duty cycle and the spin period of canonical pulsars has a large spread (Manchester et al. 2005). Moreover, it is observed that this relationship does not apply to radio-loud magnetars, which in general show larger duty cycles than what one would expect from the extrapolation of this tentative relation for radio pulsars to magnetars (see, e.g., Camilo et al. 2006, 2007). To avoid the uncertainty of beaming models, which for magnetars are mostly unknown even theoretically, we plotted the isotropic radio luminosity for all the different pulsar classes in Figure 6. From this plot, at variance with canonical radio pulsars, we see how the brightest single peaks for radio-loud magnetars might exceed their rotational powers, in line with what is possibly observed for GLEAM-X J1627. While not resolving uncertainties related to the exact mechanism of radio emission or the beaming factor, Figure 6 shows that, under the assumption of isotropic emission, even for magnetars the brightest single peaks exceed their rotational energy budget. Considering all the uncertainties in the assumptions used to derive the radio luminosities plotted in Figure 6, GLEAM-X J1627’s radio luminosity excess over its rotational power cannot be used as an argument for or against its neutron star nature.

Furthermore, in Figure 7 we report the radio-transient plane (Cordes et al. 2004; Pietka et al. 2015), where we include the

brightest radio single peaks observed in radio-loud magnetars and compare them with GLEAM-X J1627 and other classes of radio-emitting sources (data collected from Pietka et al. 2015; Marsh et al. 2016; Keane 2018, and Nimmo et al. 2022). On the x -axis we report the product of the transient emission duration (or pulse width) times the frequency at which it was observed, and on the y -axis the observed flux density times distance squared. The shaded gray area, starting from brightness temperatures of $T_b < 10^{12}$ K, divides the coherent and incoherent emission processes in the Rayleigh–Jeans approximation (Cordes et al. 2004; Pietka et al. 2015). As reported by Hurley-Walker et al. (2022), the radio emission of GLEAM-X J1627 occupies a region on the plane compatible with being powered by a coherent process, as also observed in other radio pulsars and radio-loud magnetars.

4.2. Neutron Star Cooling Models Compared With the X-Ray Upper Limits

The X-ray upper limits that we derived for GLEAM-X J1627 might be used to constrain its age and field configuration in the pulsar scenario. In particular, the magnetic field of a pulsar is expected to heat the neutron star crust via the dissipation of currents, which depends on the crustal microphysics, the pulsar magnetic field strength and configuration, and the star’s age. To compare our X-ray upper limits with neutron star cooling curves, we used a 2D magneto-thermal evolution code (Aguilera et al. 2008; Pons et al. 2009; Viganò et al. 2012; Viganò et al. 2013, 2021).

This 2D code assumes a background structure for the star in order to calculate necessary microphysical ingredients, such as

the electron density n_e , thus providing realistic magneto-thermal information. A comprehensive revision of the micro-physics embedded in magneto-thermal models is given by Potekhin et al. (2015). In this study, we have used the 2D magneto-thermal code to run a set of cooling models using different initial configurations. We considered (i) crust-confined fields, where the radial component of the magnetic field vanishes at the crust–core interface, while the latitudinal (B_θ) and toroidal (B_ϕ) components are different from zero; and (ii) core-dominated fields, where the radial component of the magnetic field is $B_r \neq 0$ at the crust–core interface, and the magnetic field lines penetrate the core. In both cases, at the stellar surface the magnetic field is matched continuously with the potential solution of a force-free field (i.e., the electric currents do not leak into the magnetosphere). The cooling models use the Sly4¹² equation of state (Douchin & Haensel 2001) with a mass of $1.4 M_\odot$ and the envelope model of Gudmundsson et al. (1983). The initial magnetic field ranges from 10^{12} G up to 10^{15} G for the dipolar poloidal component at the pole of the star, whereas the toroidal component accounts for about 40%–50% of the total magnetic energy in the system. Note that we have neglected neutrino-synchrotron cooling in these simulations, as this effect requires further examination, which is planned in the future.

Figure 8 shows a comparison of the 2D magneto-thermal models for crustal (top panel) and core-confined (bottom panel) field configurations, superimposed on the X-ray emission of different pulsar classes, in particular radio magnetars, normal X-ray-emitting pulsars, X-ray dim isolated neutron stars (XDINSs) and low-field magnetars (data updated from Viganò et al. 2013, to be published in C. Dehman et al. 2022, in preparation). In the typical scenario of a crust-confined field configuration, the X-ray limits we derive for GLEAM-X J1627 are hardly compatible with any radio magnetar known so far. Even the oldest representatives of the magnetar class, the low-field magnetars, have a quiescent emission at ages $< 10^6$ yr that is brighter than our limits for GLEAM-X J1627. On the other hand, we must remark that significant (observable) Joule heating effects in magnetars are only evident for crustal confined models: if the currents are mostly located in the neutron star core, Joule heating is very ineffective (most energy is lost through neutrino emission). Hence, any of the fast cooling mechanisms discussed in the literature may be reconciled with magnetar-like fields with very low luminosities in the core-field scenario (see Anzuini et al. 2022 for a similar discussion).

4.3. Optical/NIR Constraints and the Possible White Dwarf Nature of GLEAM-X J1627

The optical and NIR observations we report here might provide information on the possibility that GLEAM-X J1627 is a binary system harboring a slowly spinning magnetic white dwarf, given the detected radio periodicity. Radio periodic emission has so far only been observed from the white dwarf pulsar binary AR Sco (Marsh et al. 2016), although AR Sco is not known to display powerful transient radio pulses and this emission is clearly not coherent (unlike GLEAM-X J1627; see also Figure 7).

Within the $2''$ positional uncertainty, there are two optical sources, G1 and D1. Within $4''$ there are five other objects. The

Gaia parallaxes for the brighter five stars are undetermined, precluding a comparison with the radio distance of GLEAM-X J1627. Adopting an extinction A_V in the range between 1.0 and 4.1 and a distance estimate of 1.3 ± 0.5 kpc, the positions of the Gaia stars in the Gaia Hertzsprung–Russell diagram do not match the white dwarf sequence, but fall on the main sequence of mid/late-type stars for $A_V = 1$ and 2, or below it for $A_V = 4$ (see also the left panel of Figure 9). Indeed, the optical spectra acquired at SALT for G1, G3, and G4, the optical colors, and the absence of detection in the u' band suggest that these optical sources are mid/late-type stars (see the left panel of Figure 9, where the positions of the five Gaia objects are shown in black for $A_V = 4.1$ and in magenta for $A_V = 1$). Assuming their tentative spectral types and taking into account the uncertainty in the extinction, we can place lower limits on the distances of these Gaia stars adopting the corresponding V -band absolute magnitudes and the Gaia DR3 conversion formulas¹³: for G1 $d > 3.7$ kpc, for G2 $d > 3.9$ kpc, for G3 $d \geq 1.6$ kpc, for G4, and for G5 $d > 2.2$ kpc. We also note that the distances obtained for these Gaia sources by Bailer-Jones et al. (2021) using a Galactic prior model give lower limits of 3–4 kpc. We therefore conclude that these stars are unlikely to be emitting white dwarfs, and that only source G3 and possibly sources G4 and G5 might have distances compatible with GLEAM-X J1627. Similar conclusions were drawn using the Gaia proper motions and constructing a reduced proper motion diagram given the large uncertainties in extinctions, expected absolute magnitudes, and proper motions. However, this does not rule out the possibility of these sources being mid/late-type companion stars of a binary white dwarf system similar to AR Sco. Given our NIR limits, we can only rule out such a system for $A_V \leq 2$.

The distances of the faint objects D1 and D2 cannot be constrained either. Their SEDs indicate that they are cool objects with temperatures between 3000 and 7300 K (see Figure 5). If they were main-sequence stars, their distances would be > 3.3 kpc for D1 and > 4.4 kpc for D2. Therefore, we can reliably exclude that they are companion stars of a white dwarf binary system. Similarly, the hypothesis that GLEAM-X J1627 could be a hot and bright magnetic sub-dwarf star located at 1.3 kpc (Loeb & Maoz 2022) would be difficult to reconcile with the lack of detection in the DECAPS survey. We also note that the hot sub-dwarf stars (sdO/B type) identified by Gaia within 1.5 kpc have absolute magnitudes between -1 and 7 in the G band (Geier et al. 2019) and are typically not highly magnetic. At the estimated distance of GLEAM-X J1627, such a star would have been detected.

The possibility that GLEAM-X J1627 may be an isolated magnetic white dwarf pulsar located at 1.3 kpc is less constrained. Such a star would only be detected in the optical/NIR observations if it is hot (with a temperature $> 10,000$ K) and has a low extinction of $A_V \sim 2$. The right panel of Figure 9 shows the masses and temperatures of detected isolated magnetic white dwarfs with our DECAPS limit ($r > 22.9$) superimposed as a dotted line (Vennes et al. 2011; Kawka & Vennes 2012; Ferrario et al. 2020). Therefore, we cannot rule out a scenario of an isolated, cooler white dwarf.

¹² <https://compose.obspm.fr/>

¹³ See Table 5.8 of the Gaia DR3 data guide (<https://gea.esac.esa.int/archive/documentation/GDR3/>).

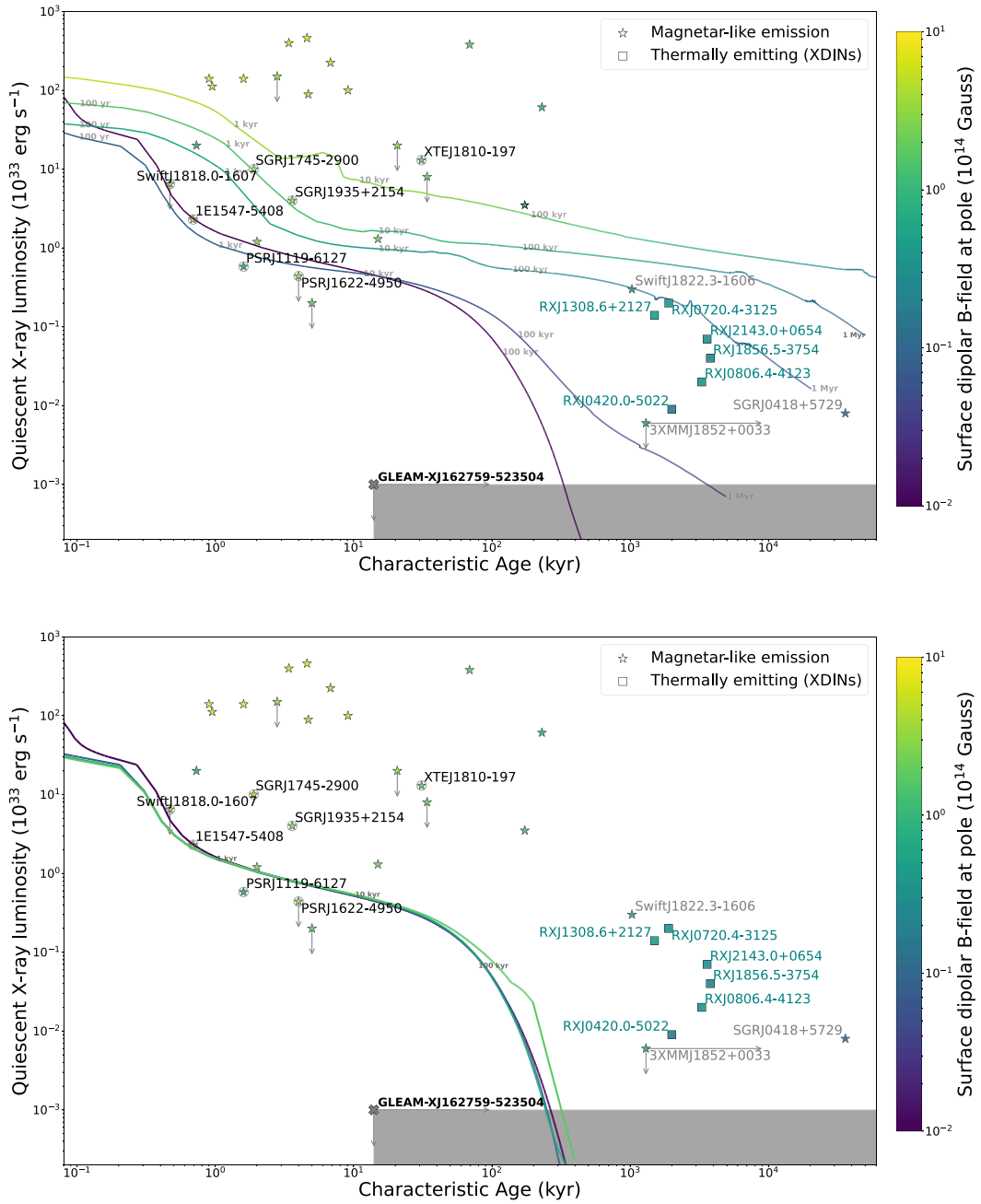


Figure 8. Evolutionary tracks for crust-dominated (top panel) and core-dominated (bottom panel) B -field configurations superimposed on the X-ray luminosity of different pulsar classes, in particular radio-loud magnetars (labeled using a gray circle), XDINs (in light blue), and low-field magnetars (labeled using gray names). The shaded region corresponds to the limits on the X-ray luminosity and the characteristic age derived for GLEAM-X J1627.

5. Conclusions

In the magnetar scenario, the upper limits we have derived on the X-ray luminosity ($L_X < 10^{30}$ erg s $^{-1}$) imply that GLEAM-X J1627’s age should be >1 Myr for any reasonable crustal magnetic field ($B > 10^{13}$ G). The 18 min spin period (assuming a fast rotating pulsar at birth) would necessarily require a strong magnetic field and a phase of fossil-disk accretion (see Ronchi et al. 2022), but in any case the age of GLEAM-X J1627 is constrained to be two orders of magnitude higher than that of typical radio-loud magnetars (which have ages <20 kyr). At this age, the bright radio bursts emitted by GLEAM-X J1627 would be unusual for such an old magnetar. However, it is important to note that the radio emission of

GLEAM-X J1627 is instead in line with what has been observed for the known population of radio-loud magnetars (which are younger). The excess of its radio luminosity over the rotational power limits is not unprecedented in the bright single pulses from radio magnetars, despite the unavoidable uncertainty due to the radio beaming factor (see Figure 6). We also note that, if the magnetar has a core-dominated magnetic field or has witnessed unusual fast cooling (both effects have never been unambiguously observed in a pulsar or a magnetar), the observed X-ray upper limits would be compatible with a younger age (see Figure 8). The field in the core is expected to decay on timescales of 1–10 Myr, hence the source’s spin period would initially evolve with a seemingly constant

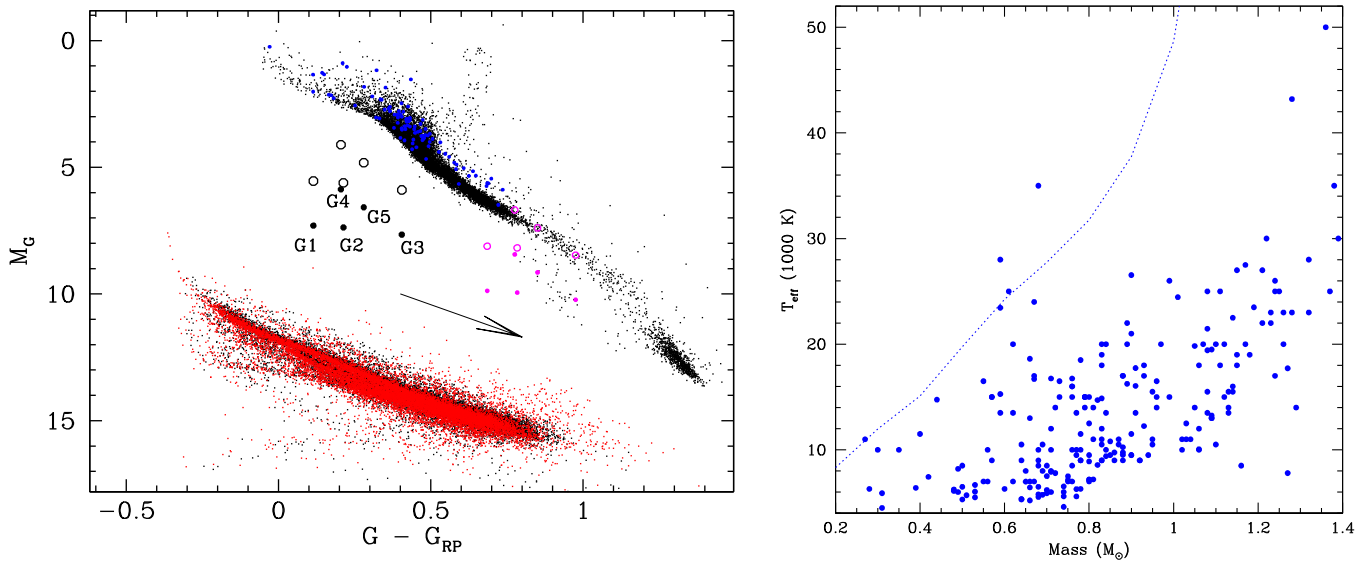


Figure 9. Left panel: color–magnitude diagram of the five Gaia stars adopting a distance range between 0.8 kpc (filled circles) and 1.8 kpc (empty circles), and extinctions $A_V = 1.0$ (magenta) and $A_V = 4.1$ (black). The small dots represent the stars in the color–magnitude diagram retrieved from the Gaia DR3 archive within 100 pc and negligible extinction ($A_G < 0.04$). Those flagged as non-single stars are shown in blue. The white dwarfs within 100 pc from the Gaia DR2 catalog of Torres et al. (2019) are reported as black dots, and the white dwarfs within 100 pc from the Gaia EDR3 catalog with a probability $>90\%$ of being a white dwarf (Gentile Fusillo et al. 2021) are reported as red dots. An extinction vector $A_V = 2$ is also reported. Right panel: mass and temperature for known magnetic isolated white dwarfs from Ferrario et al. (2020) compared to the upper limit of $r > 22.9$ at 5σ obtained by DECAM (blue dotted line).

magnetic field (see Figure 1). In this case, to explain the 18 min spin period, we would need a constant field of $B \sim 10^{15}$ G for $\sim 10^8$ yr (or $B \sim 10^{16}$ G for $\sim 10^6$ yr), which is rather extreme when compared to the known magnetar population in our Galaxy. In contrast, assuming fall-back accretion, the spin period can easily be reconciled with a 18 min value (Ronchi et al. 2022). Although the core-dominated field-decay interpretation or a fast cooling scenario are in principle viable, they are intriguing, as we have no evidence of other pulsars that require either hypothesis to explain their emission and spin period.

In the magnetic white dwarf scenario, our NIR and optical studies put some constraints on the binary or isolated white dwarf interpretation of GLEAM-X J1627. In particular, none of the sources detected within its positional uncertainty could be unambiguously cataloged as a white dwarf or the companion star of a binary white dwarf system at 1.3 kpc. An AR Sco–like system could pass unnoticed if it has a relatively large extinction. Furthermore, we exclude the possibility of GLEAM-X J1627 being a hot, bright magnetic sub-dwarf star, but cannot rule out an isolated, cooler white dwarf. We note that the rotation periods of magnetic white dwarfs are typically longer than 1 hr, with a few spinning at faster rates (Kilic et al. 2021; Schwab 2021), which are believed to be the results of the merger of a double white dwarf system. Therefore a cool isolated white dwarf would need to be sufficiently magnetic, hence probably with a large mass and small radius, to produce the coherent and pulsed radio emission observed by GLEAM-X J1627.

We gratefully acknowledge the help of D. Minniti and J. Alonso-García in providing the VVVX NIR catalog in advance. We thank A. Possenti for starting the literature search for some of the bright radio magnetar single pulses presented in this work, and the anonymous referee for her/his careful reading and useful comments that improved our manuscript. N.R., F.C.Z., C.D., M.R., V.G., C.P., A.B., and E.P. are

















supported by the ERC Consolidator Grant “MAGNESIA” under grant agreement No. 817661, and National Spanish grant No. PGC2018-095512-BI00. F.C.Z., A.B., and V.G. are also supported by Juan de la Cierva Fellowships. C.D., M.R., and C. A.’s work has been carried out within the framework of the doctoral program in Physics of the Universitat Autònoma de Barcelona. N.H.W. is supported by an Australian Research Council Future Fellowship (project number FT190100231) funded by the Australian Government. D.d.M. acknowledges financial support from the Italian Space Agency (ASI) and National Institute for Astrophysics (INAF) under agreements ASI-INAF I/037/12/0 and ASI-INAF n.2017-14-H.0 and from INAF “Sostegno alla ricerca scientifica main streams dell’INAF,” Presidential Decree 43/2018 and from INAF “SKA/CTA projects,” Presidential Decree 70/2016. D.B. acknowledges support from the South African National Research Foundation. D.V. is supported by the ERC Starting Grant “IMAGINE” under grant agreement No. 948582. This work was also partially supported by the program Unidad de Excelencia Maria de Maeztu de Maeztu CEX2020-001058-M and by the PHAROS COST Action (grant No. CA16214).

This research has made use of the services of the ESO Science Archive Facility. This work has made use of data from the European Space Agency (ESA) mission Gaia (<https://www.cosmos.esa.int/gaia>), processed by the Gaia Data Processing and Analysis Consortium (DPAC; <https://www.cosmos.esa.int/web/gaia/dpac/consortium>). Funding for the DPAC has been provided by national institutions, in particular the institutions participating in the Gaia Multilateral Agreement. This work is based on data products from observations made with ESO Telescopes at the La Silla Paranal Observatory under program ID 177.D-3023, as part of the VST Photometric $H\alpha$ Survey of the Southern Galactic Plane and Bulge (VPHAS+, www.vphas.eu), and data products from VVVX Survey observations made with the VISTA telescope at the ESO Paranal Observatory under program ID 198.B-2004. The SALT observations were obtained under the SALT Large Science

Programme on transients (2018-2-LSP-001; PI: DB) which is also supported by Poland under grant No. MNiSW DIR/WK/2016/07. The MeerKAT telescope is operated by the South African Radio Astronomy Observatory, which is a facility of the National Research Foundation, an agency of the Department of Science and Innovation. The Australia Telescope Compact Array is part of the Australia Telescope National Facility (<https://www.atnf.csiro.au/>), which is funded by the Australian Government for operation as a National Facility managed by CSIRO. We acknowledge the Gomeri people as the traditional owners of the Observatory site. This scientific work makes use of the Murchison Radio-astronomy Observatory, operated by CSIRO. We acknowledge the Wajarri Yamatji people as the traditional owners of the Observatory site. Support for the operation of the MWA is provided by the Australian Government (NCRIS), under a contract to Curtin University administered by Astronomy Australia Limited. Establishment of the Murchison Radio-astronomy Observatory and the Pawsey Supercomputing Centre are initiatives of the Australian Government, with support from the Government of Western Australia and the Science and Industry Endowment Fund. We acknowledge the Pawsey Supercomputing Centre, which is supported by the Western Australian and Australian Governments. Access to Pawsey Data Storage Services is governed by a Data Storage and Management Policy (DSMP). ASVO has received funding from the Australian Commonwealth Government through the National eResearch Collaboration Tools and Resources (NeCTAR) Project, the Australian National Data Service (ANDS), and the National Collaborative Research Infrastructure Strategy.

Facilities: Chandra (ACIS-S), ATCA, Blanco Telescope (DECAPS), Gaia, MeerKAT, MWA, SALT, VISTA (VVVX), VST (VPHAS+).

ORCID iDs

N. Rea  <https://orcid.org/0000-0003-2177-6388>
 F. Coti Zelati  <https://orcid.org/0000-0001-7611-1581>
 C. Dehman  <https://orcid.org/0000-0003-0554-7286>
 N. Hurley-Walker  <https://orcid.org/0000-0002-5119-4808>
 D. De Martino  <https://orcid.org/0000-0002-5069-4202>
 A. Bahramian  <https://orcid.org/0000-0003-2506-6041>
 D. A. H. Buckley  <https://orcid.org/0000-0002-7004-9956>
 J. Brink  <https://orcid.org/0000-0003-0030-7566>
 A. Kawka  <https://orcid.org/0000-0002-4485-6471>
 J. A. Pons  <https://orcid.org/0000-0003-1018-8126>
 D. Viganò  <https://orcid.org/0000-0001-7795-6850>
 V. Graber  <https://orcid.org/0000-0002-6558-1681>
 M. Ronchi  <https://orcid.org/0000-0003-2781-9107>
 C. Pardo Araujo  <https://orcid.org/0000-0002-8118-255X>
 A. Borghese  <https://orcid.org/0000-0001-8785-5922>
 E. Parent  <https://orcid.org/0000-0002-0430-6504>

References

- Aguilera, D. N., Pons, J. A., & Miralles, J. A. 2008, *ApJL*, 673, L167
 Alonso-García, J., Saito, R. K., Hempel, M., et al. 2018, *A&A*, 619, A4
 Anzuini, F., Melatos, A., Dehman, C., Viganò, D., & Pons, J. A. 2022, *MNRAS*, 509, 2609
 Babusiaux, C., Fabricius, C., Khanna, S., et al. 2022, arXiv:2206.05989
 Bailer-Jones, C. A. L., Rybizki, J., Fousneau, M., Demleitner, M., & Andrae, R. 2021, *AJ*, 161, 147
 Briggs, D. S. 1995, AAS Meeting, 27, 112.02
 Brinkworth, C. S., Burleigh, M. R., Lawrie, K., Marsh, T. R., & Knigge, C. 2013, *ApJ*, 773, 47
 Buckley, D. A. H., Barnes, S. I., Burgh, E. B., et al. 2008, *Proc. SPIE*, 7014, 701407
 Buckley, D. A. H., Swart, G. P., & Meiring, J. G. 2006, *Proc. SPIE*, 6267, 62670Z
 Burgh, E. B., Nordsieck, K. H., Kobulnicky, H. A., et al. 2003, *Proc. SPIE*, 4841, 1463
 Caleb, M., Heywood, I., Rajwade, K., et al. 2022, *NatAs*, 6, 828
 Camilo, F., Cognard, I., Ransom, S. M., et al. 2007, *ApJ*, 663, 497
 Camilo, F., Ransom, S. M., Halpern, J. P., et al. 2006, *Natur*, 442, 892
 Cordes, J. M., Lazio, T. J. W., & McLaughlin, M. A. 2004, *NewAR*, 48, 1459
 Coti Zelati, F., Rea, N., Pons, J. A., Campana, S., & Esposito, P. 2018, *MNRAS*, 474, 961
 D’Ai, A., Evans, P. A., Gehrels, N., et al. 2016, *ATel*, 9180, 1
 Deller, A. T., Camilo, F., Reynolds, J. E., & Halpern, J. P. 2012, *ApJL*, 748, L1
 Douchin, F., & Haensel, P. 2001, *A&A*, 380, 151
 Drew, J. E., Gonzalez-Solares, E., Greimel, R., et al. 2014, *MNRAS*, 440, 2036
 Erkut, M. H. 2022, *MNRAS*, 514, L41
 Esposito, P., Rea, N., Borghese, A., et al. 2020, *ApJL*, 896, L30
 Esposito, P., Rea, N., & Israel, G. L. 2021, in *Timing Neutron Stars: Pulsations, Oscillations and Explosions*, ed. T. M. Belloni, M. Méndez, & C. Zhang (Berlin: Springer), 97
 Ferrario, L., Wickramasinghe, D., & Kawka, A. 2020, *AdSpR*, 66, 1025
 Fukugita, M., Ichikawa, T., Gunn, J. E., et al. 1996, *AJ*, 111, 1748
 Gaia Collaboration, Brown, A. G. A., Vallenari, A., et al. 2021, *A&A*, 649, A1
 Garmire, G. P., Bautz, M. W., Ford, P. G., Nousek, J. A., & Ricker, G. R., Jr. 2003, *Proc. SPIE*, 4851, 28
 Gavriil, F. P., Gonzalez, M. E., Gotthelf, E. V., et al. 2008, *Sci*, 319, 1802
 Gehrels, N. 1986, *ApJ*, 303, 336
 Geier, S., Raddi, R., Gentile Fusillo, N. P., & Marsh, T. R. 2019, *A&A*, 621, A38
 Gençali, A. A., Ertan, Ü., & Alpar, M. A. 2022, *MNRAS*, 513, L68
 Geng, J.-J., Zhang, B., & Huang, Y.-F. 2016, *ApJL*, 831, L10
 Gentile Fusillo, N. P., Tremblay, P. E., Cukanovaite, E., et al. 2021, *MNRAS*, 508, 3877
 González-Fernández, C., Hodgkin, S. T., Irwin, M. J., et al. 2018, *MNRAS*, 474, 5459
 Göğüş, E., Lin, L., Kaneko, Y., et al. 2016, *ApJL*, 829, L25
 Gudmundsson, E. H., Pethick, C. J., & Epstein, R. I. 1983, *ApJ*, 272, 286
 Han, J. L., Wang, C., Wang, P. F., et al. 2021, *RAA*, 21, 107
 He, C., Ng, C. Y., & Kaspi, V. M. 2013, *ApJ*, 768, 64
 Hewett, P. C., Warren, S. J., Leggett, S. K., & Hodgkin, S. T. 2006, *MNRAS*, 367, 454
 Hurley-Walker, N., Galvin, T. J., Duchesne, S. W., et al. 2022, *PASA*, 39, e035
 Hurley-Walker, N., Zhang, X., Bahramian, A., et al. 2022, *Natur*, 601, 526
 Jacoby, G. H., Hunter, D. A., & Christian, C. A. 1984, *ApJS*, 56, 257
 Kaspi, V. M., & Beloborodov, A. M. 2017, *ARA&A*, 55, 261
 Kawka, A., & Vennes, S. 2012, *A&A*, 538, A13
 Keane, E. F. 2018, *NatAs*, 2, 865
 Kilic, M., Kosakowski, A., Moss, A. G., Bergeron, P., & Conly, A. A. 2021, *ApJL*, 923, L6
 Loeb, A., & Maoz, D. 2022, *RNAAS*, 6, 27
 Lower, M. E., Shannon, R. M., Johnston, S., & Bailes, M. 2020, *ApJL*, 896, L37
 Lynch, R. S., Archibald, R. F., Kaspi, V. M., & Scholz, P. 2015, *ApJ*, 806, 266
 Lyne, A. G., Manchester, R. N., & Taylor, J. H. 1985, *MNRAS*, 213, 613
 Majid, W. A., Pearlman, A. B., Dobreva, T., et al. 2017, *ApJL*, 834, L2
 Manchester, R. N., Hobbs, G. B., Teoh, A., & Hobbs, M. 2005, *AJ*, 129, 1993
 Manchester, R. N., & Taylor, J. H. 1977, *Pulsars* (San Francisco, CA: W. H. Freeman)
 Marsh, T. R., Gänsicke, B. T., Hümmerich, S., et al. 2016, *Natur*, 537, 374
 Minniti, D., Lucas, P. W., Emerson, J. P., et al. 2010, *NewA*, 15, 433
 Nimmo, K., Hessels, J. W. T., Kirsten, F., et al. 2022, *NatAs*, 6, 393
 O’Donoghue, D., Buckley, D. A. H., Balona, L. A., et al. 2006, *MNRAS*, 372, 151
 Offringa, A. R., McKinley, B., Hurley-Walker, N., et al. 2014, *MNRAS*, 444, 606
 Pearlman, A. B., Majid, W. A., Prince, T. A., Kocz, J., & Horiuchi, S. 2018, *ApJ*, 866, 160
 Pietka, M., Fender, R. P., & Keane, E. F. 2015, *MNRAS*, 446, 3687
 Pons, J. A., Miralles, J. A., & Geppert, U. 2009, *A&A*, 496, 207
 Potekhin, A. Y., Pons, J. A., & Page, D. 2015, *SSRv*, 191, 239
 Rea, N., Borghese, A., Esposito, P., et al. 2016, *ApJL*, 828, L13
 Rea, N., & Esposito, P. 2011, *High-Energy Emission from Pulsars and their Systems* (Berlin: Springer), 247

- Ronchi, M., Rea, N., Graber, V., & Hurley-Walker, N. 2022, *ApJ*, **934**, 184
- Sault, R. J., Teuben, P. J., & Wright, M. C. H. 1995, in ASP Conf. Ser. 77, *Astronomical Data Analysis Software and Systems IV*, ed. R. A. Shaw, H. E. Payne, & J. J. E. Hayes (San Francisco, CA: ASP), 433
- Schlafly, E. F., & Finkbeiner, D. P. 2011, *ApJ*, **737**, 103
- Schlafly, E. F., Green, G. M., Lang, D., et al. 2018, *ApJS*, **234**, 39
- Schwab, J. 2021, *ApJ*, **906**, 53
- Sokolowski, M., Colegate, T., Sutinjo, A. T., et al. 2017, *PASA*, **34**, e062
- Straižys, V., & Lazauskaitė, R. 2009, *BaltA*, **18**, 19
- Tan, C. M., Bassa, C. G., Cooper, S., et al. 2018, *ApJ*, **866**, 54
- Tingay, S. J., Goeke, R., Bowman, J. D., et al. 2013, *PASA*, **30**, e007
- Tong, H. 2022, arXiv:2204.01957
- Torres, S., Cantero, C., Rebassa-Mansergas, A., et al. 2019, *MNRAS*, **485**, 5573
- Vasisht, G., & Gotthelf, E. V. 1997, *ApJL*, **486**, L129
- Vennes, S., Kawka, A., & Németh, P. 2011, *MNRAS*, **410**, 2095
- Viganò, D., García-García, A., Pons, J. A., Dehman, C., & Graber, V. 2021, *CoPhC*, **265**, 108001
- Vigano, D., Pons, J. A., & Miralles, J. A. 2012, *CoPhC*, **183**, 2042
- Viganò, D., Rea, N., Pons, J. A., et al. 2013, *MNRAS*, **434**, 123
- Wayth, R. B., Tingay, S. J., Trott, C. M., et al. 2018, *PASA*, **35**, e033
- Weltevrede, P., Johnston, S., & Espinoza, C. M. 2011, *MNRAS*, **411**, 1917
- Wilson, W. E., Ferris, R. H., Axtens, P., et al. 2011, *MNRAS*, **416**, 832
- Yao, J. M., Manchester, R. N., & Wang, N. 2017, *ApJ*, **835**, 29